Available online at www.sciencedirect.com
ScienceDirect
Sensors and Actuators A 137 (2007) 147–156
SENSORS AND ACTUATORS A PHYSICAL
www.elsevier.com/locate/sna

A single input–single output mass sensor based on a coupled array of microresonators

Barry E. DeMartini [a], Jeffrey F. Rhoads [b,*], Steven W. Shaw [b], Kimberly L. Turner [a]

[a] *Department of Mechanical and Environmental Engineering, University of California-Santa Barbara, Santa Barbara, CA 93106, United States*
[b] *Department of Mechanical Engineering, Michigan State University, East Lansing, MI 48824, United States*

Received 14 October 2006; received in revised form 13 February 2007; accepted 14 February 2007
Available online 17 February 2007

Abstract

This paper summarizes the results of a joint analytical and experimental investigation of a new class of resonant microsensors. The key feature of these devices is that they exploit vibration localization in a set of functionalized, frequency mistuned microbeam resonators, each coupled to a common shuttle mass, to facilitate the detection of multiple analytes using a single sensor input and a single sensor output (measurement readout). The work details a wide variety of issues related to the development of such a sensor, with particular emphasis placed on the formulation of a representative lumped-mass model for the sensor, the analysis of the sensor model's frequency response, preliminary experimental results, which verify the feasibility of the proposed sensor design, and pertinent design and integration issues.

Keywords: MEMS; Resonant sensor; Chemical and biological sensors; Mass sensor; Localization; Coupled oscillators

1. Introduction

In the past decade, resonant microsystems have been proposed for use in a wide variety of chemical and biological sensing applications, including those relating to public health and safety (e.g., in biological detectors capable of monitoring the environment for compounds such as mercury), medical research and diagnostics (e.g., in detectors capable of identifying the presence of a certain protein or strand of DNA), and national security and defense (e.g., in sensors capable of detecting the presence of chemical or biological agents or explosive compounds) [1–14]. While this broad applicability has stimulated some interest, the principal interest in such systems stems largely from the inherent advantages MEMS-based sensor platforms have over their macroscale counterparts, namely, they are significantly smaller, consume minimal power, can be easily integrated with electronics, offer the potential for higher sensitivities, and, when mass produced, can be fabricated at a comparatively low cost. To date, most resonant microsensors have operated on a resonance tracking principle. That is, the resonant frequency of the sensor, typically comprised of an isolated, single-degree-of-freedom (SDOF) oscillator, is determined prior to implementation, and then during the course of operation the location of this resonance is tracked. As shifts in the resonant frequency are attributable to mass or stiffness changes in the oscillator, caused by absorption, desorption, local stress stiffening, or a similar chemomechanical process, these shifts can, in turn, be used to identify the presence of a target analyte [15–17]. Unfortunately, since existing microsensors typically feature a single dominant degree-of-freedom and a very limited number of analytes can be uniquely detected with a single active surface, sensors utilizing this approach are generally capable of detecting only a lone analyte (or a class of closely related analytes). Arrays of uncoupled oscillators, each individually functionalized for the detection of a specific analyte, have been implemented to overcome this limitation, but the greater hardware and signal processing requirements associated with such sensors lead to added expense and complexity [16].

This work details a novel sensor design that allows for the detection of multiple analytes using a single sensor input and a single sensor output. Specifically, these sensors utilize an architecture in which a number of frequency-mistuned microbeam resonators, each individually functionalized for the detection of a specific analyte, are attached to a common shuttle mass

* Corresponding author. Tel.: +1 517 432 1085; fax: +1 517 353 1750.
E-mail address: rhoadsje@msu.edu (J.F. Rhoads).

0924-4247/$ – see front matter © 2007 Elsevier B.V. All rights reserved.
doi:10.1016/j.sna.2007.02.011

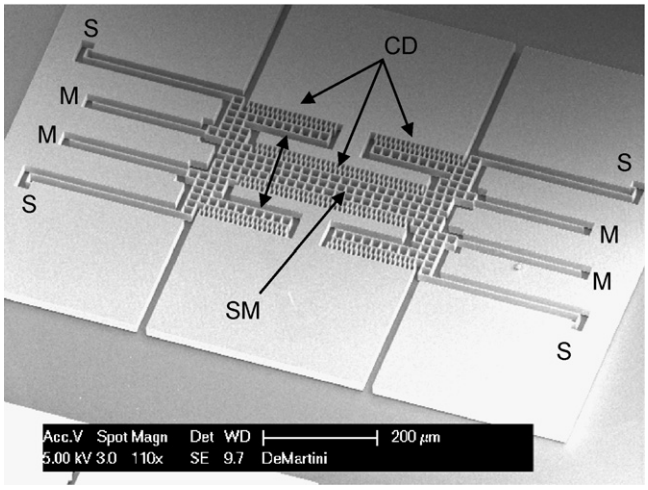

Fig. 1. A scanning electron micrograph of a translational, SISO, multi-analyte sensor. Key device features have been labeled for reference purposes as follows: the device's shuttle mass is labeled SM; the four individual microbeam oscillators are each labeled M; the electrostatic comb drives are labeled CD; and each of the four-folded beam flexures are denoted with an S. Also note that the principal direction of motion is designated by the included double-pointed arrow.

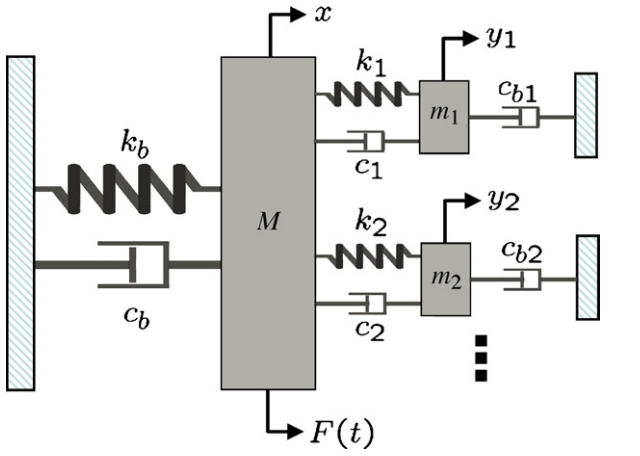

Fig. 2. A mass-spring-dashpot analog of the sensor topology depicted in Fig. 1[18,19]. Note that the larger mass M represents the sensor's shuttle mass and the comparatively smaller masses m_1, m_2, etc., represent the microbeam oscillators.

(see Fig. 1), which, in turn, is used for both actuation and sensing (measurement readout) purposes. Providing sufficient vibration localization in the set of mistuned oscillators, this innovative architecture allows for frequency shifts in any, or all, of the individual microbeams to be measured using solely the response of the common shuttle mass. Accordingly, a single, single input–single output (SISO) device proves sufficient for the detection of multiple target analytes.

This paper details a recently completed analytical and experimental investigation of the SISO microsensor design described above. The work begins with a brief overview of the device's topology, and proceeds with the derivation of a representative lumped-mass system model and a preliminary analysis of a desirable form of the sensor's frequency response. Experimental results, including those acquired from a simulated mass detection event, are then detailed. The work concludes with a brief examination of sensor metrics, a discussion of pertinent design and integration issues, and a detailed outline of future work.

2. System modeling

Though a variety of geometries can be developed based on the sensor topology described herein, the translational design depicted in Fig. 1 was selected for examination here due to its relative simplicity. As shown, this design consists of a single shuttle mass (SM) which is suspended above the substrate by four-folded beam flexures in such a way that in-plane, unidirectional motion is dominant. Actuation is provided electrostatically through one bank of interdigitated comb drives (CD) (though not presently utilized, the second bank can be used for sensing (measurement readout)). In final implementations, active sensing surfaces will be individually deposited on each of the four microbeam oscillators (M) (this number could easily be expanded to facilitate the detection of a larger number of analytes), which are attached to the common shuttle mass. It should be noted that each of these microbeams deviate slightly in length to ensure ample separation of the coupled system's resonant frequencies, which is necessary to ensure sufficient localization.

Given the geometric complexity of the sensor design depicted in Fig. 1, it proves convenient for analysis to model the device using a simple lumped-mass analog, such as that shown in Fig. 2. Here the shuttle mass is represented by the larger mass denoted M and the microbeams are represented by the comparatively smaller masses designated m_1, m_2, etc., elasticity is captured by the linear spring elements designated k_b (for the primary system) and k_1, k_2, etc. (for the microbeams), and intrinsic and extrinsic dissipation (arising primarily from aerodynamic effects, but also including material dissipation) are captured by the linear dashpot elements designated c_b (for the primary system) and c_1, $c_{\mathrm{b}1}$, c_2, $c_{\mathrm{b}2}$, etc. (for the microbeams). The net electrostatic force, which is applied solely to the shuttle mass, is denoted by the forcing term $F(t)$. Though this topology is believed to be novel in the sensors community, it is important to note that topologies akin to that presented here have been studied in unrelated contexts, namely, broad-band noise control and vibration suppression [20–22].

Using the lumped-mass model depicted in Fig. 2, it can be shown that the equations of motion governing the system depicted in Fig. 1 are given by

$$M\ddot{x} + \sum_i m_i(\ddot{x} + \ddot{z}_i) + \sum_i c_{\mathrm{b}i}(\dot{x} + \dot{z}_i) + c_\mathrm{b}\dot{x} + k_\mathrm{b}x = F(t), \tag{1}$$

$$m_i(\ddot{x} + \ddot{z}_i) + c_{\mathrm{b}i}(\dot{x} + \dot{z}_i) + c_i\dot{z}_i + k_i z_i = 0, \quad i = 1, \ldots, N, \tag{2}$$

where z_i is the relative displacement of the ith subsystem, given by

$$z_i = y_i - x, \quad i = 1, \ldots, N, \tag{3}$$

N specifies the number of microbeam subsystems (active sensing elements) attached to the shuttle mass, and x and y_i represent the absolute displacements of the shuttle mass and ith subsystem, respectively. Providing ample device thickness (approximately 10 μm or larger) and minimal fringe field effects, the applied electrostatic force $F(t)$, which appears in Eq. (1), can be approximated by

$$F(t) = \frac{\varepsilon_0 n h V^2(t)}{g}, \tag{4}$$

where ε_0 represents the free space permittivity, n the total number of comb fingers in the electrostatic comb banks, g the gap between adjacent comb fingers, and h the device thickness. Given a harmonic voltage excitation with amplitude V_A and frequency ω, the resulting net force features both ac and dc components and takes the form:

$$F(t) = \frac{\varepsilon_0 n h V_A^2}{2g}(1 + \cos 2\omega t) = F_0(1 + \cos 2\omega t). \tag{5}$$

The explicit appearance of the dc excitation can be resolved by redefining the dynamic variables x and z_i by translation according to

$$\hat{x} = x - \bar{x} = x - \frac{F_0}{k_b}, \qquad \hat{z}_i = z_i. \tag{6}$$

Nondimensionalizing the resulting displacements by a characteristic length of the system x_0 (e.g., the maximum allowable shuttle mass displacement, as limited by the interdigitated comb drives—note that the selection of the characteristic length is largely arbitrary due to the linear nature of the system) according to

$$u = \frac{\hat{x}}{x_0}, \qquad v_i = \frac{\hat{z}_i}{x_0} \tag{7}$$

and the system's excitation and natural frequencies by a characteristic frequency of the system ω_0 (chosen here to be the uncoupled natural frequency of the longest microbeam) yields dimensionless governing equations given by

$$u'' + 2\zeta_b \Lambda u' + \Lambda^2 u = \Gamma \cos \Omega\tau - \sum_i \hat{m}_i (u'' + v_i'') - \sum_i 2\zeta_{bi} \Upsilon_i \hat{m}_i (u' + v_i'), \tag{8}$$

$$\hat{m}_i (u'' + v_i'') + 2\hat{m}_i \zeta_i \Upsilon_i v_i' + \hat{m}_i \Upsilon_i^2 v_i = -2\hat{m}_i \zeta_{bi} \Upsilon_i (u' + v_i'), \quad i = 1, \ldots, N, \tag{9}$$

with system parameters defined as in Table 1. This system of $N + 1$ equations can be compiled into a standard matrix form given by

$$MX'' + CX' + KX = \Phi(\tau) \tag{10}$$

for further analysis. Note that here X represents a compiled state vector incorporating the displacements of both the shuttle mass and the microbeam oscillators, M an effective mass matrix incorporating inertial coupling terms, C an effective damping matrix incorporating dissipative coupling terms, K an effective stiffness matrix, and $\Phi(\tau)$ an effective forcing vector, which is sparse except for the first element.

Table 1
Nondimensional parameter definitions

Parameter	Description
$\tau = \omega_0 t$	Nondimensional time
$\Omega = \frac{2\omega}{\omega_0}$	Nondimensional excitation frequency
$(\cdot)' = \frac{d(\cdot)}{d\tau}$	New derivative operator
$u = \frac{\hat{x}}{x_0}, v_i = \frac{\hat{z}_i}{x_0}$	Nondimensional displacements
$\hat{m}_i = \frac{m_i}{M}$	Inertia ratio: ith microbeam to shuttle mass
$\Lambda = \frac{\omega_b}{\omega_0} = \frac{1}{\omega_0}\sqrt{\frac{k_b}{M}}$	Frequency ratio: isolated shuttle mass to characteristic value
$\Upsilon_i = \frac{\omega_i}{\omega_0} = \frac{1}{\omega_0}\sqrt{\frac{k_i}{m_i}}$	Frequency ratio: ith isolated microbeam to characteristic value
$\zeta_b = \frac{c_b}{2\sqrt{k_b M}}$	Damping ratio: isolated shuttle mass
$\zeta_i = \frac{c_i}{2\sqrt{k_i m_i}}$	Damping ratio: ith microbeam (isolated from ground)
$\zeta_{bi} = \frac{c_{bi}}{2\sqrt{k_i m_i}}$	Pseudo-damping ratio: ith microbeam (partially isolated from shuttle)
$\Gamma = \frac{F_0}{M x_0 \omega_0^2}$	Nondimensional excitation amplitude

3. Frequency response characteristics

Using the matrix equation developed in the preceding section, Eq. (10), the response of the sensor can be easily recovered using any one of the many techniques common to linear systems theory (the impedance approach detailed in Ref. [23] was used in the preparation of this work). However, due to the large number of free parameters present in this equation ($4N + 4$), a number of qualitatively distinct responses, most of which are poorly suited for sensing, are readily obtainable. Accordingly, the present work emphasizes *one* particular form of the system's frequency response that is amenable to sensing. A qualitative representation of this response is shown in Fig. 3. Though a limited number of alternative responses will facilitate sensing, they are presently believed to be inferior to that detailed here. Accordingly, investigation of these alternatives is left for subsequent works.

Examination of the analytical frequency response plot shown in Fig. 3 reveals several features of note. First, the response includes a dominant low-frequency resonance (1) which occurs (approximately) at the resonant frequency:

$$\Omega_0 \approx \frac{1}{\omega_0}\sqrt{\frac{k_b}{M + \sum_i^N m_i}}. \tag{11}$$

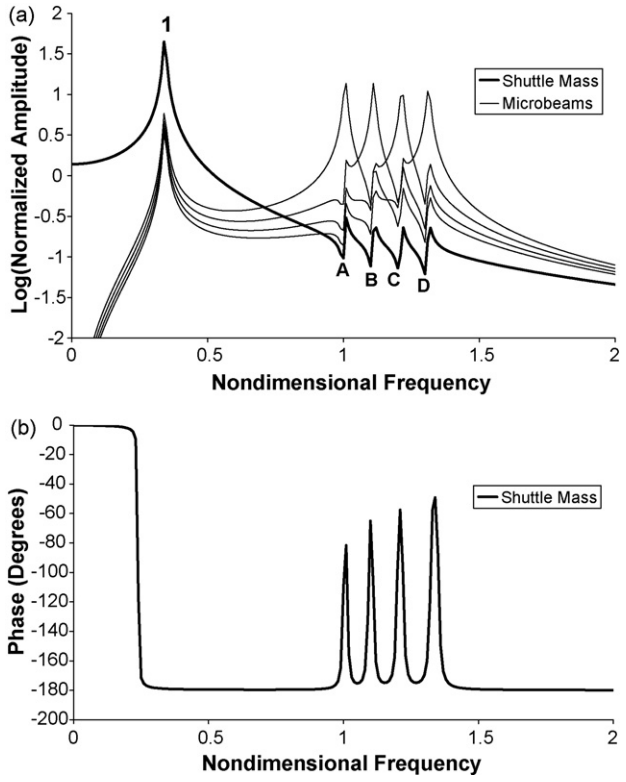

Fig. 3. A desirable form of the frequency response: (a) amplitude and (b) phase, for a representative sensor design. Note that the labeled resonances correspond to the following modes: (1) a translational in-plane mode, (A–D) modes where energy is localized in one of the sensor's microbeams. Also note that for clarity only the phase of the shuttle mass response is shown.

As modal analysis confirms, this resonance corresponds to a bulk, in-plane mode of the system where both the shuttle mass and the attached microbeam oscillators move essentially together as a lumped mass. Fig. 4a, recovered from a finite element analysis of the device verifies this modal behavior. The response also displays four additional, higher-frequency resonances, which are labeled (A)–(D). These resonances each occur at a frequency slightly greater than Υ_i, the rescaled, isolated, microbeam natural frequencies, and correspond to in-plane localized modes where appreciable displacements occur in only a single microbeam. This is confirmed not only by the comparatively larger resonant amplitudes shown in Fig. 3a, but also by the finite element results shown in Fig. 4b. It is important to note that since these higher frequency microbeam resonances (corresponding to modes where energy is largely confined in a single microbeam) induce a measurable resonance in the shuttle mass' response, resonance shifts induced by chemomechanical processes on any, or all, of the microbeams are detectable using only the shuttle mass' response. Accordingly, sweeping the excitation frequency of the system Ω through a frequency range that includes $\Upsilon_1, \ldots, \Upsilon_N$ allows for the detection of up to N distinct analytes, providing that each microbeam oscillator is properly functionalized.

In order to achieve the desired features in the shuttle mass' frequency response (depicted in Fig. 3), the system's parameters must be systematically chosen. To this end, details on the selection of inertia ratios ($\hat{m}_i$) and frequency ratios (Υ_i/Λ), as well as the amplitude of the ac voltage excitation applied to the electrostatic comb drives (V_A), which is incorporated into the nondimensional parameter Γ, are detailed here.

Careful selection of the system's frequency ratios (Υ_i/Λ) is required to ensure ample separation between all of the microsensor's resonances, including those associated with out-of-plane modes which are not captured by the lumped-mass model used in this work. To this end, the following guidelines must be observed throughout the course of design: (i) to avoid interactions between the system's low frequency resonance (labeled (1)) and the resonances associated with the localized modes (labeled (A)–(D)), the system's frequency ratios (Υ_i/Λ) must be specified to be greater than, and well separated from, unity. Failing to meet this criterion results in a contamination of the resonance peaks associated with the localized modes in the proximity of resonance (1), which can negate the successful detection of analytes using the corresponding microbeams, especially in the presence of additive noise. (ii) To avoid the potential formation of a multi-resonance passband, each Υ_i/Λ value must be distinct and well separated from all other frequency ratios. Failing to meet this criterion can result in a number of indistinct resonances, which hinders the detection of individual resonance shifts, and ultimately negates multi-analyte detection. (iii) Each uncoupled microbeam frequency Υ_i, must be well separated from the resonant frequencies associated with both out-of-plane modes and higher frequency, in-plane modes to avoid situations akin to those detailed above in case (i) where the resonances associated with the localized microbeam modes become contaminated by other system resonances. Note that since the lumped-mass model present here captures only the first five in-plane modes of the system, finite element results similar to those shown in Fig. 4 are requisite for design. Before proceeding, it should also be noted that the amount of damping present in the system greatly impacts each of the design criterion detailed above. Specifically, in low damping environments the system's resonance peaks can be placed in much closer proximity than they can be in low-Q (comparatively higher damping) environments. Accordingly, the amount of damping present in the system, not only constrains frequency ratio selection, but also ultimately limits the number of functionalized microbeams that can be integrated with the system and thus the number of distinct analytes that can be uniquely detected.

Selection of the system's inertia ratios ($\hat{m}_i$) is primarily used to control the relative coupling strength between the microbeam oscillators and the sensor's shuttle mass. Accordingly, these ratios, in conjunction with the system's frequency ratios, are used to control the extent of localization in the coupled system's response [24]. For the sensing principles discussed here, strong mode localization is necessary to ensure efficient mass sensing. This is attributable to the fact that while mass and/or stiffness changes in a single microbeam lead to shifts in all of the coupled system's resonances, in the presence of strong mode localization these mass and/or stiffness changes induce a markedly larger shift in the resonance associated with the altered oscillator. This, in turn, allows for the rapid identification of a given resonance shift's source (namely, the particular microbeam, which having

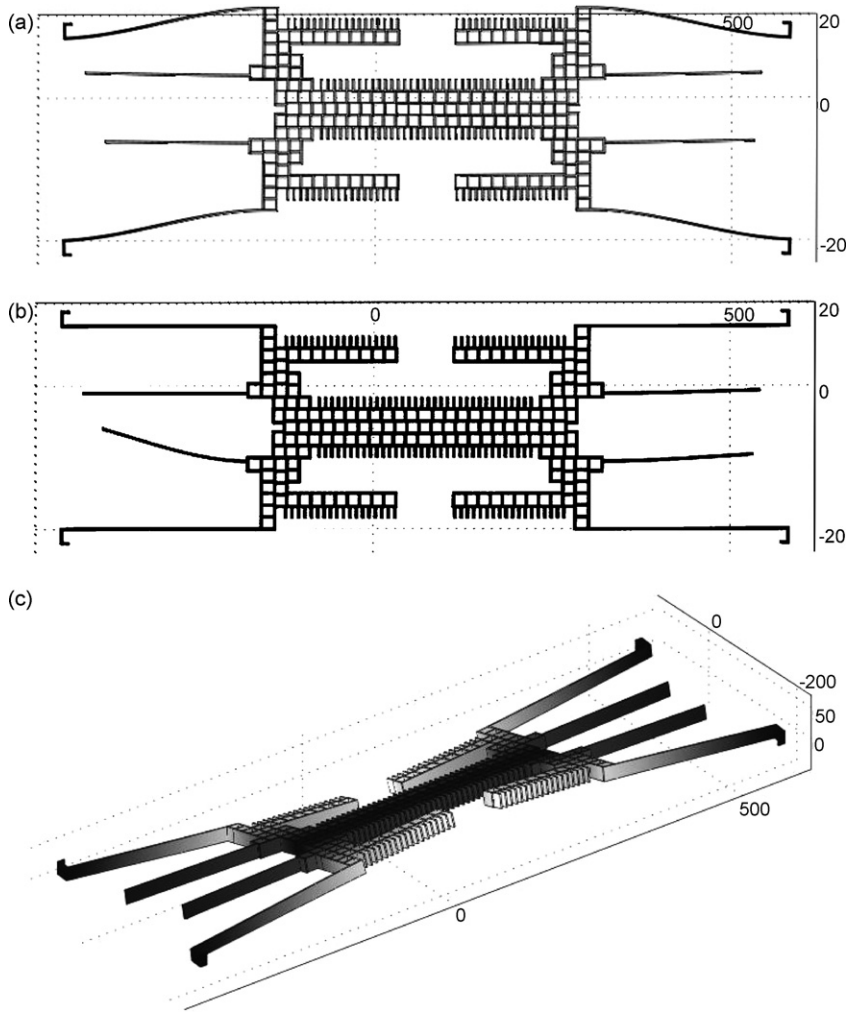

Fig. 4. Mode shapes of the sensor as recovered using computer-based finite element methods. (a) The first mode of the sensor: a bulk in-plane mode where the shuttle mass and microbeam oscillators move nearly in unison, essentially as a lumped mass. (b) The seventh mode of the sensor: an in-plane, localized mode where movement, and thus energy, is largely confined in a single microbeam. (c) The third mode of the sensor: an out-of-plane torsional mode. Note that the resonant frequencies corresponding to each of these modes are detailed in Table 2.

undergone a chemomechanical process, has had its mass and/or stiffness altered) and may ultimately facilitate automated analyte identification.

Given the linear nature of the sensor design detailed here, manipulation of the ac excitation voltage amplitude (V_A) is used primarily to control the relative magnitude of the shuttle mass' response. As it is desirable to operate in ambient pressure (low-Q) environments, harmonic signals with large excitation amplitude are generally desirable. Caution must be taken, however, to ensure that these amplitudes do not lead to nonlinear resonance structures or device burn-outs.

4. Preliminary experimental results

For proof of concept, a translational device of the type outlined in Section 2 was designed, fabricated, and tested experimentally. A scanning electron micrograph of the resulting device is shown in Fig. 1. The device was fabricated on a silicon-on-insulator (SOI) wafer with a $\approx 20\,\mu m$ device layer. The process flow included a lithographic step for pattern definition, a deep silicon etch using a deep reactive ion etcher (DRIE), an O_2 reactive ion etch (RIE) for polymer removal, and finally a hydrofluoric acid wet etch to remove the silicon dioxide beneath the oscillator [25].

For this experiment one set of the interdigitated comb drives was used for electrostatic actuation and the response of the shuttle mass was measured using a single beam laser vibrometer (Polytec) [26]. Since the vibrations of interest occurred in-plane (perpendicular to the laser beam), a 45° mirror was cut into the silicon next to the shuttle mass using a focused ion beam. The output from the vibrometer, which is directly proportional to velocity, was sent to a vector signal analyzer (Hewlett Packard 89410A) to obtain the frequency response of the shuttle mass. By actuating the device with a 6.2 V ac signal in 275 mTorr vacuum and sweeping frequency, the response of the shuttle mass shown in Fig. 5 was obtained. The experimental response contains the desired spectral features shown in Fig. 3 (namely the resonances designated (1), (A)–(D)), as well as some that were not predicted with the lumped-mass model. The desired spectral features in the experimental response are the low fre-

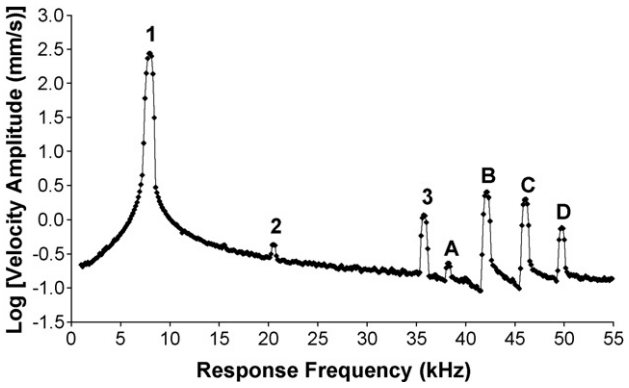

Fig. 5. Experimentally obtained frequency response for the sensor depicted in Fig. 1 actuated with a 6.2 V ac signal in 275 mTorr pressure [18,19]. Note that the labeled resonances correspond to the following modes: (1) bulk in-plane mode, (2 and 3) out-of-plane modes, and (A–D) modes where energy is localized in the sensor's microbeams. The resonant frequencies associated with each of these modes are tabulated in Table 2.

quency resonance (1), which occurred at approximately 8 kHz, corresponding to the bulk in-plane mode, and the higher frequency resonances (A)–(D), occurring between approximately 38 kHz and 50 kHz (with a spacing of about 4 kHz), corresponding to the localized microbeam modes (Fig. 4b illustrates one localized microbeam mode). All in-plane modes of oscillation were verified using stroboscopic imagining equipment from Polytec. The modes that were not predicted by the lumped-mass models (2) and (3), occurring at approximately 20 kHz and 36 kHz, were predicted by three-dimensional finite element simulations (Fig. 4c shows the characteristic shape of mode (3)) and correspond to out-of-plane modes. Note that frequency data corresponding to all of the system's resonances is tabulated in Table 2. Also note that since resonance (3) occurred close to resonance (A), there was a reduction in the resonant amplitude of (A). Due to the inherently small nature of the localized mode amplitudes, any further reduction in amplitude could be detrimental to the signal to noise ratio and therefore the performance of the sensor in practical implementation. Future sensors should be carefully designed such that all unwanted modes are sufficiently separated from the modes of interest.

To simulate mass detection the frequency response of the shuttle mass was recorded before and after the deposition of a

Table 2
A comparison between the system's experimental and theoretical (FEA) resonant frequencies

Mode	Experimental value (Hz)	FEA value (Hz)	Percent error (%)
Bulk translational mode	8,002	8,478	5.9
First out-of-plane mode	20,660	22,893	10.8
Second out-of-plane mode	35,877	40,335	12.4
First localized mode	38,301	41,435	8.2
Second localized mode	42,206	45,608	8.1
Third localized mode	46,112	49,594	7.6
Fourth localized mode	49,882	53,808	7.9
Third out-of-plane mode	–	59,226	–

Note that the discrepancy shown above is believed to be caused by uncertainties in the device's material properties and thickness.

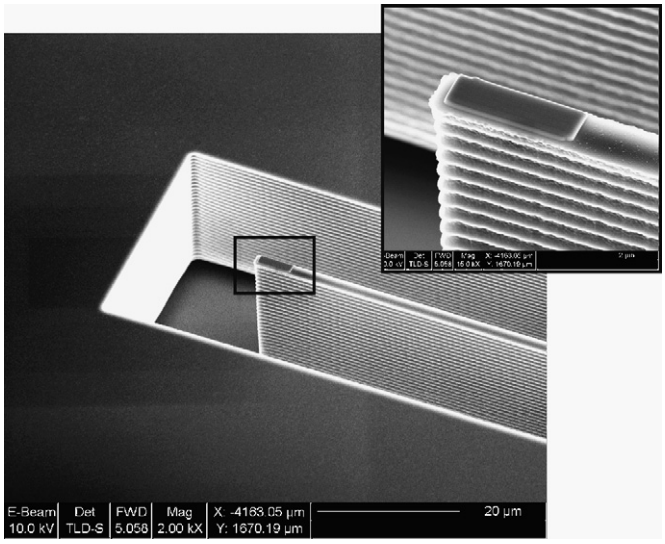

Fig. 6. A scanning electron micrograph of the platinum patch added to the shortest microbeam [18,19]. The inset, which was used for measurement purposes, shows a closer view. The patch measures approximately 1.57 μm × 5.10 μm × 0.22 μm in size and has a mass of approximately 38 pg, as computed volumetrically.

small patch of platinum onto the highest frequency microbeam. The platinum patch (shown in Fig. 6), deposited using a focused ion beam, measured 1.57 μm × 5.10 μm × 0.22 μm and had an approximate mass of 38 pg. (Note, this patch was added to the tip of the microbeam so that the effective stiffness was unaffected.) The responses of the shuttle mass measured before and after deposition (zoomed in on the four resonances corresponding to the localized microbeam modes) are shown in Fig. 7. It is apparent that resonance (D), the localized mode of the highest frequency microbeam (the mass loaded microbeam), has been altered much more than resonances (A)–(C). A higher resolution sweep near resonance (D), shown in Fig. 8, reveals a shift of 124 Hz. Performing the same high resolution sweep near resonance (C), shown in Fig. 9, reveals a much smaller shift of 3 Hz, which is 40 times smaller than that of the loaded microbeam.

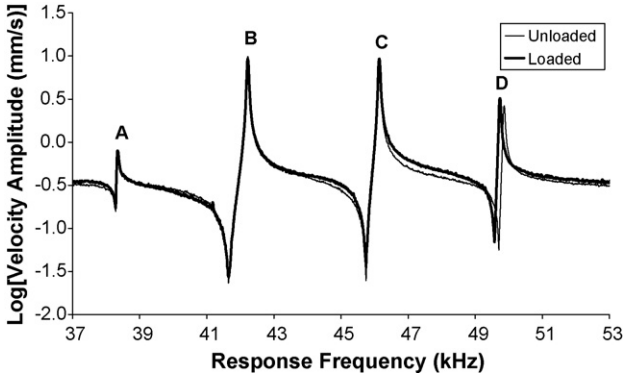

Fig. 7. Experimentally obtained frequency response for the sensor depicted in Fig. 1 actuated with a 12.2 V ac signal in 275 mTorr pressure [18,19]. Note that the added-mass loading introduces shifts in each of the system's resonances, the largest of which occurs in resonance (D), which corresponds to the localized mode of the corresponding beam. Here, and in Figs. 8 and 9, individual data points have been removed for clarity.

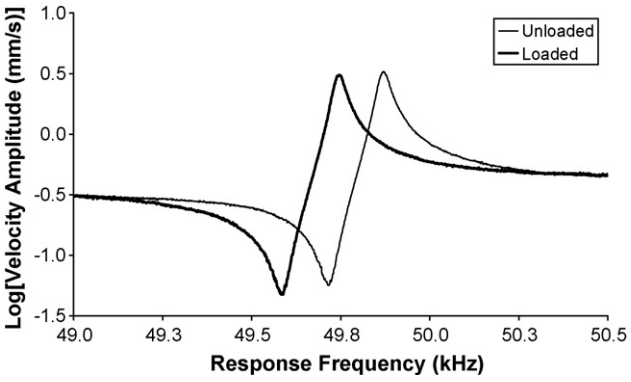

Fig. 8. Experimentally obtained frequency response near resonance (D) for the sensor depicted in Fig. 1 actuated with a 12.2 V ac signal in 275 mTorr pressure [18,19]. Note that the mass loading introduces a resonance shift of approximately 124 Hz.

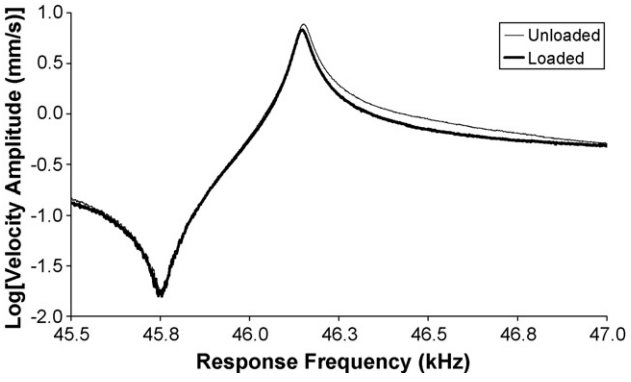

Fig. 9. Experimentally obtained frequency response near resonance (C) for the sensor depicted in Fig. 1 actuated with a 12.2 V ac signal in 275 mTorr pressure [18,19]. Note that the mass loading introduces a resonance shift of approximately 3 Hz.

The markedly larger shift in the mass loaded microbeam resonance as compared to the unloaded microbeam resonances is a direct results of strong mode localization.

5. Sensor metrics

In order to quantify the performance of the device presented here, and ultimately facilitate comparison between it and other resonant mass sensors, a few representative metrics are considered. An approach akin to that presented in Ref. [27] is adopted and extended to accommodate the system's multiple degrees of freedom.

For mass sensors, the most pertinent performance metric is a measure of the smallest added mass that can be accurately detected using the given device, or the sensor's so-called mass sensitivity. In the case of resonant devices, this measure can be represented as the product of two independent metrics: mass responsivity (actually its inverse), which quantifies the extent to which a system's resonant frequency will change with a small mass addition; and frequency resolution, which specifies the smallest frequency shift that can be accurately measured in the presence of noise and uncertainty. Assuming that sensor/analyte interactions result solely in mass addition (the subsequent discussion can be easily extended to account for stiffness changes in applications where stiffness contributions are non-negligible), the mass sensitivity of a SDOF mass sensor can be approximated by

$$\partial m \approx S^{-1} \partial \omega_0, \tag{12}$$

where S is the device's mass responsivity and $\partial\omega_0$ is the system's frequency resolution. For the multi-degree-of-freedom (MDOF) sensor detailed here this can be extended to account for N resonance shifts induced by up to N mass changes. This results in a mass sensitivity vector, Δm, given by

$$\Delta m \approx \mathbf{S}^{-1} \Delta \omega, \tag{13}$$

where $\mathbf{S}$ represents the square $(i \times j)$ mass responsivity matrix, which is composed of elements that quantify the shift in ith resonance of the system due to mass addition at the jth oscillator, and the vector $\Delta\omega$ dictates the frequency resolution associated with each of the system's resonances.

The mass responsivity matrix $\mathbf{S}$ associated with the device shown in Fig. 1 can be partially compiled using the experimental results detailed in the previous section. For example, the (5, 5) element of the matrix, corresponding to the mass responsivity of resonance (D) with respect to a mass addition to the highest frequency microbeam, can be computed to be 3.3 Hz/pg. Similarly, the mass responsivity associated with resonance (C) computed with respect to a mass addition on the highest frequency microbeam, which corresponds to the matrix's (4, 5) element, can be shown to be approximately 0.1 Hz/pg. Extending this procedure through further experimentation will reveal a diagonally dominant mass responsivity matrix. This can be attributed to the localized nature of the response, which, as detailed in the previous section, leads to significantly larger shifts in the resonances associated with the localized modes of the mass loaded microbeams (as compared to those shifts induced solely through coupling).

It is important to note that though the experimentally determined mass responsivity of the mass loaded microbeam is comparable to other reported values for resonant multi-analyte sensors, these values are significantly lower than those reported for sensors based on isolated microresonators [14,16,28]. Though much of this difference can be attributed to the larger scale of the devices considered here and can be rectified through device scaling, it is important to note that the mass responsivities of these devices (and microsensors based on coupled system architectures, in general) will always be slightly inferior to those of other microsensors (i.e. those based on isolated microresonators). This is due to the inter-oscillator coupling, which manifests itself in the off-diagonal terms of the responsivity matrix, which in the presence of added mass leads to small shifts in each of the system's resonances, not just that associated with the localized mode of the altered beam. Current design studies, the results of which will be incorporated into second-generation devices, are aimed at minimizing these off-diagonal terms while still allowing for the measurement of the response of a common shuttle mass that supports the individual sensor elements.

Despite the fact that thermomechanical noise, absorption–desorption noise, temperature fluctuations, and other factors known to contribute to a system's frequency resolution have been studied in the context of SDOF resonant mass sensors (see, for example, [27]), to the best of the authors' knowledge, the impact of these effects in coupled oscillator systems has thus far not been considered. As such, present understanding facilitates, at best, a conservative estimate of the frequency resolution(s) associated with the sensor/experimental setup described herein. Currently, the frequency resolution is believe to be limited by the resolution of the spectrum analyzer/laser vibrometer system detailed in Section 4 and thus a conservative frequency resolution estimate of 1.5 Hz, which is significantly larger than the smallest frequency shift measurable with the experimental setup, is assumed for each of the system's resonances. This results in sub-picogram mass sensitivities for the sensor in its current experimental configuration. In final device implementations, however, additional hardware components, such as phase locked loops, may appreciably alter this resolution. As such, on-going studies are aimed at extending the results of Ref. [27] to MDOF devices in hopes of refining this approximation.

6. Design and integration issues

Though the preliminary results detailed thus far in the present work are believed to be a positive indication of the feasibility of the SISO, multi-analyte sensor, a number of design and integration issues must still be addressed prior to the implementation of these devices. The following subsections detail the most pertinent issues.

6.1. Response measurement

A fundamental issue that must be addressed in the design of any second-generation, SISO, multi-analyte sensor is the method of response measurement. In the present work, all of the included data was recovered optically through laser vibrometry. However, for most applications this laboratory-based technique is impractical. An obvious alternative is to utilize the unused sets of electrostatic comb drives incorporated in the original device design in a capacitive detection scheme. However, the capacitance differences induced by the displacement of the shuttle mass, even during near-resonant operation, are of insufficient magnitude (approximately 0.4 fF) to be accurately measured with off-chip electronics. On-chip CMOS electronics may facilitate the detection of these small differential capacitances, but the exploitation of alternative transduction mechanisms is likely a more practical approach. Presently, the authors are considering the integration of piezoelectric or magnetomotive elements into second-generation designs. Both of these techniques yield readily attainable, response-proportional voltages and have been successfully integrated in micro- and nano-scale devices in other contexts [29,30].

6.2. System integration

Highly intertwined with the design issues detailed in the previous section is the integration of the resonant microsensor with integrated or external circuitry capable of measuring the resonance shifts induced in the system's response during analyte detection. Currently, phase locked loops are exploited for such purposes, but it is not readily apparent that such circuits will suffice (or be efficient) for MDOF systems that exhibit multiple resonance shifts. Ongoing research is aimed at examining this approach, as well as a number of alternatives, including the post-processing of acquired data using computer algorithms.

6.3. The inclusion of additional sensing elements

Though the device design described in Section 4 is capable of detecting up to four distinct analytes, full exploitation of the SISO, multi-analyte sensor concept requires the inclusion of additional sensing elements (microbeams). Accordingly, the next generation of SISO sensors is slated to incorporate ten or more uniquely functionalized microbeams. While this increased value of N is readily obtainable with careful design, it is important to note that there are practical constraints on the number of microbeams implementable in a single sensor. Specifically, given a non-resonant frequency window of bandwidth B, the number of microbeam resonances (and thus the number of microbeams) that can fit within the specified band, can be approximated by

$$N_{\max} \approx \frac{BQ_{\text{nom}}}{\omega_{\text{nom}}}, \tag{14}$$

where ω_{nom} and Q_{nom} represent the nominal frequency (e.g. the mean resonant frequency of the localized microbeam modes) and quality factor (e.g. the mean Q value, computed with respect to half-power points) associated with the coupled microbeam resonances, respectively. In the event that $N_{\max}$ proves insufficient for a given application, it may be possible to exploit multiple non-resonant frequency bands. This, however, will require extremely careful design and relatively tight constraints on both geometric and material property uncertainty.

6.4. Environmental issues

Though the device examined herein operated successfully in a partial vacuum environment (275 mTorr), simulated mass detection proved unsuccessful at 1 atm. While mass sensing in partial vacuum may be suitable for some applications, the vast majority will require that the device operate in ambient pressures. Accordingly, the next generation of SISO, multi-analyte sensors must be designed to operate in ambient environmental conditions. In the present device, fluid pumping between the microbeam oscillators and the sidewalls of the device's substrate is believed to be the primary limiting factor. This can likely be remedied in second-generation devices through device scaling, the removal of excess substrate material, and geometrical reconfiguration. More radical changes, including the use of alternative geometries and/or employing feedback control [31] or parametric amplification [32], may be worth consideration if these changes prove insufficient.

6.5. Surface functionalization

As detailed in Section 4, mass addition was realized in this work via the deposition of a small platinum patch on one of the sensor's microbeams. However, in implementation the system's microbeam oscillators will have to be functionalized with chemically selective surface layers. Given the considerable amount of research which has focused on the development of chemically active surfaces for use in microcantilever sensors (see, for example, [9,10,12,33,34]), the present intent is to adopt one of the many previously developed functionalization schemes in second-generation, SISO devices to realize the detection of multiple analytes.

7. Conclusion

This work summarizes the preliminary results of a joint analytical and experimental investigation of a new class of resonant microsensors. The key feature of these devices is that they exploit vibration localization in a set of functionalized, frequency-mistuned microbeam resonators, each coupled to a common shuttle mass, to facilitate the detection of multiple analytes using a single sensor input and a single sensor output (measurement readout). Though a wide variety of issues are discussed in the work, particular emphasis is placed on the formulation of a representative lumped-mass model for the sensor, the analysis of a representative form of the sensor's frequency response, preliminary experimental results, and pertinent design issues. Analytical results were used to show that N distinct resonance shifts could be detected using solely the response of a single shuttle oscillator, provided N frequency mistuned microbeam oscillators were attached, and this was subsequently verified experimentally.

Though the sensor detailed in the work performed as expected, the investigation did reveal a number of design and integration issues that must be considered in subsequent investigations. Amongst the more pertinent issues was the need for a MDOF frequency resolution model, improved sensor performance in ambient pressure environments, and refined measurement methods. Each of these issues, as well as others, are presently being considered.

Acknowledgements

This work was supported by the National Science Foundation under grant NSF-0428916. Portions of this work were presented at Hilton Head 2006: A Solid State Sensors, Actuators and Microsystems Workshop [18] and the 2006 ASME International Mechanical Engineering Congress and Exposition [19].

References

[1] F.M. Battiston, J.P. Ramseyer, H.P. Lang, M.K. Baller, C. Gerber, J.K. Gimzewski, E. Meyer, H.J. Guntherodt, A chemical sensor based on a microfabricated cantilever array with simultaneous resonance-frequency and bending readout, Sens. Actuators B 77 (1/2) (2001) 122–131.

[2] Z.J. Davis, G. Abadal, O. Kuhn, O. Hansen, F. Grey, A. Boisen, Fabrication and characterization of nanoresonating devices for mass detection, J. Vac. Sci. Tech. B 18 (2) (2000) 612–616.

[3] K.L. Ekinci, X.M.H. Huang, M.L. Roukes, Ultrasensitive nanoelectromechanical mass detection, Appl. Phys. Lett. 84 (22) (2004) 4469–4471.

[4] B. Ilic, D. Czaplewski, H.G. Craighead, P. Neuzil, C. Campagnolo, C. Batt, Mechanical resonant immunospecific biological detector, Appl. Phys. Lett. 77 (3) (2000) 450–452.

[5] N. Nugaeva, K.Y. Gfeller, N. Backmann, H.P. Lang, M. Duggelin, M. Hegner, Micromechanical cantilever array sensors for selective fungal immobilization and fast growth detection, Biosens. Bioelect. 21 (6) (2005) 849–856.

[6] T. Ono, X. Li, H. Miyashita, M. Esashi, Mass sensing of adsorbed molecules in sub-picogram sample with ultrathin silicon resonator, Rev. Sci. Instrum. 74 (3) (2003) 1240–1243.

[7] R. Raiteri, M. Grattarola, H.-J. Butt, P. Skladal, Micromechanical cantilever-based biosensors, Sens. Actuators B 79 (2/3) (2001) 115–126.

[8] L.B. Sharos, A. Raman, S. Crittenden, R. Reifenberger, Enhanced mass sensing using torsional and lateral resonances in microcantilevers, Appl. Phys. Lett. 84 (23) (2004) 4638–4640.

[9] M. Su, S. Li, V.P. Dravid, Microcantilever resonance-based DNA detection with nanoparticle probes, Appl. Phys. Lett. 82 (20) (2003) 3562–3564.

[10] T. Thundat, E.A. Wachter, S.L. Sharp, R.J. Warmack, Detection of mercury vapor using resonating microcantilevers, Appl. Phys. Lett. 66 (13) (1995) 1695–1697.

[11] A. Zribi, A. Knobloch, W.-C. Tian, S. Goodwin, Micromachined resonant multiple gas sensor, Sens. Actuators A 122 (1) (2005) 31–38.

[12] H.P. Lang, R. Berger, F. Battiston, J.-P. Ramseyer, E. Meyer, C. Andreoli, J. Brugger, P. Vettiger, M. Despont, T. Mezzacasa, L. Scandella, H.-J. Guntherodt, C. Gerber, J.K. Gimzewski, A chemical sensor based on a micromechanical cantilever array for the identification of gases and vapors, Appl. Phys. A 66 (Suppl. 1) (1998) S61–S64.

[13] K.Y. Gfeller, N. Nugaeva, M. Hegner, Micromechanical oscillators as rapid biosensor for the detection of active growth of *Escherichia coli*, Biosens. Bioelect. 21 (3) (2005) 528–533.

[14] Y.T. Yang, C. Callegari, X.L. Feng, K.L. Ekinci, M.L. Roukes, Zeptogram-scale nanomechanical mass sensing, Nano Lett. 6 (4) (2006) 583–586.

[15] G.Y. Chen, T. Thundat, E.A. Wachter, R.J. Warmack, Adsorption-induced surface stress and its effects on resonance frequency of microcantilevers, J. Appl. Phys. 77 (6) (1995) 3618–3622.

[16] H.P. Lang, M. Hegner, C. Gerber, Cantilever array sensors, Mater. Today 8 (4) (2005) 30–36.

[17] Q. Ren, Y.-P. Zhao, Influence of surface stress on frequency of microcantilever-based biosensors, Microsyst. Tech. 10 (4) (2004) 307–314.

[18] B.E. DeMartini, J.F. Rhoads, S.W. Shaw, K.L. Turner, A resonant SISO sensor based on a coupled array of microelectromechanical oscillators, in: Proceedings of Hilton Head 2006: A Solid-state Sensor, Actuator, and Microsystems Workshop, Hilton Head, SC, 2006.

[19] J.F. Rhoads, B.E. DeMartini, S.W. Shaw, K.L. Turner, A SISO, multi-analyte sensor based on a coupled microresonator array, in: Proceedings of the 2006 ASME International Mechanical Engineering Conference and Exposition, Chicago, IL, 2006.

[20] G. Maidanik, K.J. Becker, Noise control of a master harmonic oscillator coupled to a set of satellite harmonic oscillators, J. Acoust. Soc. Am. 104 (5) (1998) 2628–2637.

[21] K. Xu, T. Igusa, Dynamic characteristics of multiple substructures with closely spaced frequencies, Earth Eng. Struct. Dyn. 21 (12) (1992) 1059–1070.

[22] R.L. Weaver, Mean and mean-square responses of a prototypical master/fuzzy structure, J. Acoust. Soc. Am. 101 (3) (1997) 1441–1449.

[23] L. Meirovitch, Elements of Vibration Analysis, 2nd ed., McGraw-Hill, New York, 1986.

[24] C. Pierre, E.H. Dowell, Localization of vibrations by structural irregularity, J. Sound Vib. 114 (3) (1987) 549–564.

[25] W. Zhang, W. Zhang, K. Turner, P.G. Hartwell, SCREAM'03: A single mask process for high-Q single crystal silicon MEMS, in: Proceedings of the 2004 ASME International Mechanical Engineering Congress and Exposition, Anaheim, CA, 2004.

[26] K.L. Turner, P.G. Hartwell, N.C. MacDonald, Multi-dimensional MEMS motion characterization using laser vibrometry, in: Proceedings of Transducers '99: The 10th International Conference on Solid-state Sensors and Actuators, Sendai, Japan, 1999, pp. 1144–1147.
[27] K.L. Ekinci, Y.T. Yang, M.L. Roukes, Ultimate limits to inertial mass sensing based upon nanoelectromechanical systems, J. Appl. Phys. 95 (5) (2004) 2682–2689.
[28] B. Ilic, D. Czaplewski, M. Zalalutdinov, H.G. Craighead, P. Neuzil, C. Campagnolo, C. Batt, Single cell detection with micromechanical oscillators, J. Vac. Sci. Tech. B 19 (6) (2001) 2825–2828.
[29] A.N. Cleland, Foundations of nanomechanics: from solid-state theory to device applications, in: Advanced Texts in Physics, Springer, Berlin, 2003.
[30] P. Mohanty, D.A. Harrington, K.L. Ekinci, Y.T. Yang, M.J. Murphy, M.L. Roukes, Intrinsic dissipation in high-frequency micromechanical resonators, Phys. Rev. B 66 (2000) 085416.
[31] J. Tamayo, A.D.L. Humphris, A.M. Malloy, J.M. Miles, Chemical sensors and biosensors in liquid environment based on microcantilevers with amplified quality factor, Ultramicroscopy 86 (1/2) (2001) 167–173.
[32] D. Rugar, P. Grütter, Mechanical parametric amplification and thermomechanical noise squeezing, Phys. Rev. Lett. 67 (6) (1991) 699–702.
[33] H.P. Lang, R. Berger, C. Andreoli, J. Brugger, M. Despont, P. Vettiger, C. Gerber, J.P. Ramseyer, E. Meyer, H.-J. Guntherodt, Sequential position readout from arrays of micromechanical cantilever sensors, Appl. Phys. Lett. 72 (3) (1998) 383–385.
[34] T. Thundat, G.Y. Chen, R.J. Warmack, D.P. Allison, E.A. Wachter, Vapor detection using resonating microcantilevers, Anal. Chem. 67 (3) (1995) 519–521.

Biographies

Barry E. DeMartini received a BS Degree in Mechanical Engineering from the University of California, Santa Barbara in 2003. He is currently working toward a PhD degree in Mechanical Engineering at the same institution. His research interests include resonant mass sensors for chemical and biological detection, design and characterization of micro/nanoscale resonators, and nonlinear dynamics and chaos in microelectromechanical systems. He is a student member of the Institute of Electrical and Electronics Engineers (IEEE).

Jeffrey F. Rhoads received both the BS (2002) and MS (2004) degrees in mechanical engineering from Michigan State University. He is currently working toward the PhD degree at the same institution. His research interests include the nonlinear behavior of parametrically excited systems and coupled oscillators, as well as the predictive design and analysis of resonant microelectromechanical systems (MEMS). He is a student member of the American Society of Mechanical Engineers (ASME).

Steven W. Shaw received his AB in physics and his MS in applied mechanics from the University of Michigan in 1978 and 1979, respectively, and the PhD in theoretical and applied mechanics from Cornell in 1983. He is currently a professor in the Department of Mechanical Engineering at Michigan State University, where he has been since 1984. He has held visiting appointments at Caltech, the University of Michigan, the University of Minnesota, and the University of California-Santa Barbara. His interests are in the general area of engineering dynamical systems, including applications in MEMS, rotating machinery, vehicle dynamics, and structural vibrations. Dr. Shaw is a fellow of the American Society of Mechanical Engineers (ASME), a member of the Society of Automotive Engineers (SAE), and a member the American Academy of Mechanics. He is past recipient of the ASME Henry Hess Award and the SAE Arch T. Colwell Merit Award. He serves as a contributing editor for Nonlinear Dynamics, and on the editorial boards for the Journal of Sound and Vibration and Communications in Nonlinear Science and Numerical Simulation.

Kimberly L. Turner received the BS degree in mechanical engineering from Michigan Technological University in 1994 and the PhD degree in theoretical and applied mechanics from Cornell University, Ithaca, NY, in 1999. She is currently an associate professor of mechanical and environmental engineering at the University of California, Santa Barbara, where she has served on the faculty since 1999. Her research interests include nonlinear dynamics of micro/nanoscale systems, testing and characterization of MEMS devices, modeling of micro/nanoscale devices, and solid-state sensor development. Dr. Turner is a member of American Society of Mechanical Engineers (ASME), SEM, AVS, and the Cornell Society of Engineers. She has received the NSF CAREER award, and the Varian Award from the AVS.